

Experimental characterization of two-axis MEMS scanners with hidden radial vertical combdrive actuators and cross-bar spring structures

Jui-che Tsai¹, Tien-liang Hsieh¹, Chun-da Liao¹, Sheng-jie Chiou¹,
Dooyoung Hah² and Ming C Wu³

¹ Graduate Institute of Photonics and Optoelectronics and Department of Electrical Engineering, National Taiwan University, Taipei 10617, Taiwan

² Department of Electrical and Computer Engineering, Louisiana State University, Baton Rouge, LA 70803, USA

³ Department of Electrical Engineering and Computer Sciences and Berkeley Sensor and Actuator Center (BSAC), University of California–Berkeley, Berkeley, California 94720-1774, USA

E-mail: jtsai@cc.ee.ntu.edu.tw

Received 30 October 2008, in final form 26 January 2009

Published 11 March 2009

Online at stacks.iop.org/JMM/19/045002

Abstract

In this paper, we perform the experimental characterization of two-axis MEMS scanners driven by radial vertical combdrive actuators. The dc scan ranges are limited by the pull-in effect. Each scanner utilizes a cross-bar spring structure to achieve two rotational degrees of freedom (DOFs) without employing any gimbal. Both the actuators and torsion springs are hidden underneath the mirror to obtain a small form factor. The devices are fabricated by a five-layer polysilicon surface micromachining process (SUMMiT-V). Devices with different combinations of parameter values are experimentally characterized and compared.

(Some figures in this article are in colour only in the electronic version)

1. Introduction

Two-axis micromirrors have been one of the focus areas in the field of optical micro-electro-mechanical systems (MEMS). They enable two-dimensional (2D) beam steering and have numerous applications in optical fiber communication, display technologies and biological imaging and tomography, etc. Two-axis micromirror arrays have been successfully incorporated into three-dimensional (3D) optical cross connects (OXC)s [1–3] and wavelength-selective switches (WSSs) [4] in fiber optical networks. They provide the modules with fast switching speeds, low optical insertion loss, and independence of the wavelength and polarization. Two-axis scanners can also be found in display systems. For example, a projection display system, such as the laser scanning display (LSD) [5] or retinal scanning display (RSD) [6], comprises a laser source and a single dual-axis MEMS

scanner. It scans the laser beam in two dimensions to generate the images. In the area of biomedical imaging, a miniaturized optical scanning head can be manufactured by packaging a two-axis MEMS scanner into an endoscopic form [7].

Electrostatic actuation has been one of the most popular driving mechanisms for two-axis MEMS scanners. It offers several advantages such as high reliability, low power consumption, fast response time, simple device structures and good compatibility with the fabrication process of integrated circuits. Although parallel-plate electrostatic actuators [8, 9] exhibit the simplest structures among all types of electrostatic actuators, their traveling ranges are restricted by the pull-in effect. By contrast, combdrive actuators [10–14] prevail as ideally they are free from the pull-in effect and also offer larger force densities.

As for the two rotational degrees of freedom that a dual-axis combdrive-driven scanner should possess, normally a

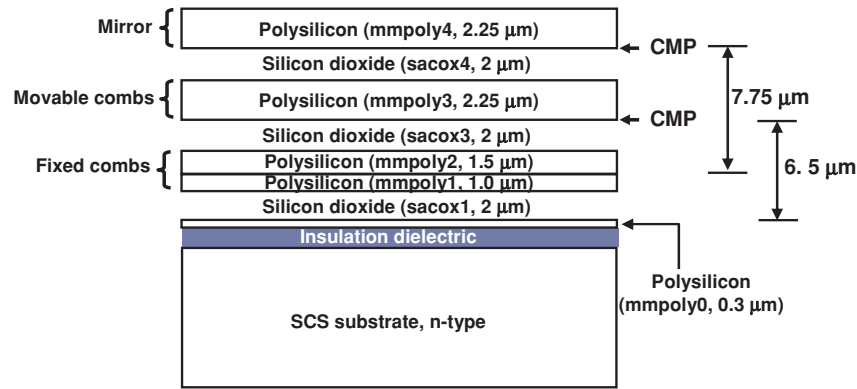


Figure 1. SUMMiT-V structural and sacrificial layers.

gimbal structure is employed to achieve them [15]. However, the gimbal usually occupies a significant area, thus resulting in a relatively large device form factor. It also leads to an undesired small fill factor when replicating the mirror to form an array. Therefore, it is preferable to eliminate the gimbal structure. Several two-axis gimbal-less scanners were demonstrated. Tip-tilt-piston micromirrors, which utilized mechanical linkages and rotation transformers to operate without the use of any gimbal, were developed by Milanović *et al* [16]. However, they were fabricated by a bulk micromachining process which required multiple-wafer bonding, and their dimensions, up to a few hundred microns, were difficult to reduce. Another gimbal-less MEMS mirror with two-axis tilting and vertical piston motions was achieved by the leverage mechanism in conjunction with the combdrive actuators [17]. The device was made by a three-structural-layer polysilicon surface micromachining process, and a mirror size of $120 \mu\text{m} \times 120 \mu\text{m}$ was feasible. Nevertheless, a high voltage of 110 V was required just to reach a 4° mechanical tilt.

We propose combining radial vertical combdrive actuators with a cross-bar spring structure [8] to eliminate the need of a gimbal in a two-axis scanner. The orthogonal torsion springs provide the two desired rotational degrees of freedom. The combdrive actuators generate a large force density and therefore reduce the driving voltage. Both the actuators and spring structure are hidden under the mirror to reduce the device form factor for a given mirror area. This further helps in achieving a high fill factor when replicating such a scanner to form a 1D or a 2D array. This design concept was first revealed in [18], demonstrating a successful working device. We later performed the theoretical analyses of several design variants in [19], where two selected devices were tested for experimental verification. Recently, we incorporated a modification that employed a balanced spring structure to obtain equal x - and y -axis scan ranges [20]. In this paper, we present the experimental characterization of all the 19 design variants, which as a whole exhibit three types of cross-bar spring structures and different initial finger gaps, finger lengths and finger overlap lengths. Comparisons will be made based on the experimental data.

2. Design and fabrication

2.1. Sandia Ultra-Planar, Multi-Level MEMS Technology V (SUMMiT-V) process

The Sandia Ultra-planar, Multi-level MEMS Technology V (SUMMiT-V) process is used to fabricate our devices. It is a five-layer polycrystalline silicon surface micromachining process, which provides four mechanical layers of polysilicon (mmpoly1–mmpoly4) above a thin polysilicon electrical interconnect and ground plane layer (mmpoly0). All of them are built on top of a single crystal silicon (SCS) wafer coated with a layer of insulation dielectric ($0.63 \mu\text{m}$ thermal oxide + $0.80 \mu\text{m}$ silicon nitride). A typical full stack and the nominal layer thicknesses are shown in figure 1.

The polysilicon is deposited with LPCVD and doped with phosphorous. TEOS silicon dioxide (denoted by sacox in figure 1) is used as the sacrificial material. Silicon dioxide right beneath the top two levels of polysilicon, i.e. sacox4 and sacox3, is planarized using a chemical mechanical polishing (CMP) process, which eliminates the topography resulting from the earlier steps of fabrication.

2.2. Design

2.2.1. Device structures. Figure 2 is the schematic drawing of the device, which is imaginarily disassembled for a clearer illustration. The mmpoly0 layer is used for the interconnecting lines, voltage feed-through lines/planes for the fixed combs and shielding ground planes. The shielding ground planes minimize the area of exposed dielectric, which makes the mirror immune from drift related to the dielectric charging effect. The fixed combs and the movable combs are made of the laminated mmpoly1+mmpoly2 stack ($2.5 \mu\text{m}$ thick) and the mmpoly3 layer, respectively. The top polysilicon layer, mmpoly4 ($2.25 \mu\text{m}$ thick), is used for the mirror. The spacing between the mirror and substrate is $10.75 \mu\text{m}$.

Our design includes several variants. They are categorized into three groups based on their cross-bar spring structures, as shown in figure 3. For the type I devices, the lower and upper torsion springs of the cross-bar structure, which provide the mechanical restoring torques about the x and y -axes,

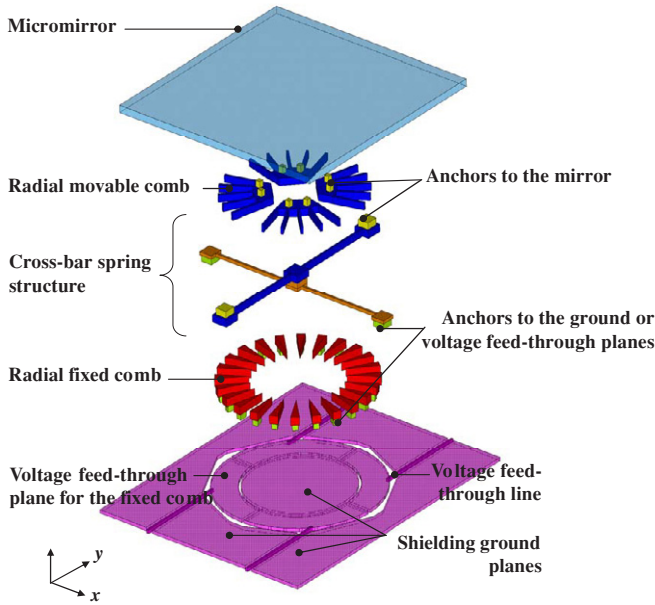


Figure 2. Schematic illustration of the two-axis MEMS scanner with radial vertical combdrive actuators and a cross-bar spring structure [19].

respectively, are made of mmpoly1 and mmpoly3 layers. This unique multilayer spring structure enables us to achieve large clearance for both rotational modes: $6.5 \mu\text{m}$ ($2 \mu\text{m} + 2.5 \mu\text{m} + 2 \mu\text{m}$) and $7.75 \mu\text{m}$ ($1.5 \mu\text{m} + 2 \mu\text{m} + 2.25 \mu\text{m} + 2 \mu\text{m}$) for x - and y -axis rotations, respectively, as indicated in figure 1. The type II devices bear a similar spring design except that a double-beam architecture is employed to implement the lower springs for improvement of the lateral stability. The type III devices use the same layer (mmpoly1) for both the x - and y -axis torsion springs. The spacing between the torsion

springs and shielding ground planes (mmpoly0) is fixed at $2 \mu\text{m}$ (i.e. the thickness of sacox1), which is the clearance for the x -axis rotation. Therefore, the spring length has to be reduced to maintain a sufficient angular scan range.

For each device, the mirror, movable combs and torsion springs are mechanically and electrically connected together through anchors. They are always grounded during operation as the spring structure is anchored to the shielding planes. The scanner is equipped with four quadrantly arranged sets of fixed combs, each anchored to its own voltage feed-through plane. Therefore, a maximum of four independent voltages can be applied. In addition, various comb parameter values are adopted, and they are listed in table 1 of the following section along with the spring dimensions.

2.2.2. Device parameters. The torsion beam widths are all set as $1 \mu\text{m}$ in the design layout. The initial finger gap of any certain device is either $1 \mu\text{m}$, $2 \mu\text{m}$ or $3 \mu\text{m}$, with the movable finger width fixed at $1 \mu\text{m}$. The finger length and finger overlap vary from device to device. The size of the square mirror is $96 \mu\text{m} \times 96 \mu\text{m}$. The dimensions are chosen for the MEMS wavelength-selective switch, which normally requires a 1D array of micromirrors with a size of $100\text{--}200 \mu\text{m}$ [4]. The mirror alone can be extended for other applications without changing the dimensions of the actuators and springs.

Figure 4 shows the scanning electron microscopy (SEM) photographs of the fabricated devices. The images are taken after a 45 min HF release process of oxide etching and CO_2 supercritical drying. The central device of figure 4(a) is a standard one with a square mirror. Figure 4(b) is the close-up view of a mirror which is intentionally cut into a circular shape to reveal the underlying structures and for examination of the pull-in mechanism. For the square-mirror device, the gutter-like structures work as on-chip shadow masks that prevent electrical shorting between electrodes after the post-release

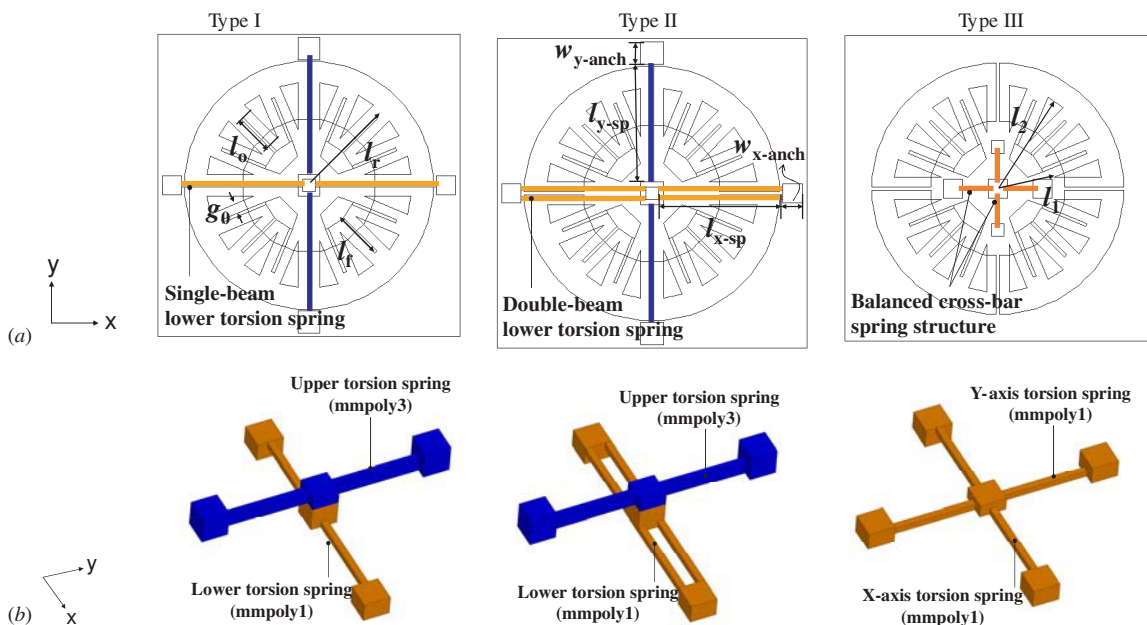


Figure 3. Schematic drawings of the three types of cross-bar spring structures: (a) top views and (b) oblique views.

Table 1. Device parameters.

Device number	l_{x-sp}/w_{x-anch} (μm)	l_{y-sp}/w_{y-anch} (μm)	g (μm)	l_1 (μm)	l_2 (μm)	l_o (μm)	l_f (μm)	l_r (μm)
Type I: devices with single-beam lower springs								
A1			1	17.21	32.51	12.79	15.5	30
B2			1	25.04	32.51	4.95	10.0	30
A2 ^a			1	25.04	32.51	4.95	10.0	30
E1			2	19.15	32.55	10.85	13.5	30
B1	37.5/6	36.5/7	2	23.13	32.55	6.86	9.5	30
D1			3	17.94	32.56	12.06	15.0	30
E2			3	22.26	32.56	7.72	10.0	30
C1			3	17.94	36.97	20.06	23.0	38
D2			3	22.26	36.97	12.74	15.0	35
C2 ^a			3	22.26	36.97	12.74	15.0	35
Type II: devices with double-beam lower springs								
D3			1	17.21	32.51	12.79	15.5	30
C3			1	25.04	32.51	4.95	10.0	30
E6	37.5/6	36.5/7	2	19.15	32.55	10.85	13.5	30
E5			2	23.13	32.55	6.86	9.5	30
E4			3	17.94	32.56	12.06	15.0	30
E3			3	22.26	32.56	7.72	10.0	30
Type III: devices with balanced cross-bar spring structures								
S1	12/6	12/4	1	17.21	32.51	12.80	15.5	30
S2	12/6	12/4	2	19.15	32.55	10.85	13.5	30
S3	8/6	8/4	3	17.94	32.56	12.07	15.0	30

l_{x-sp} : length of the x -axis torsion spring,

l_{y-sp} : length of the y -axis torsion spring,

w_{x-anch} : width of the anchor of the x -axis torsion spring,

w_{y-anch} : width of the anchor of the y -axis torsion spring,

g : initial gap spacing between the movable and fixed fingers,

l_1 : distance from the device center to the fixed finger tip,

l_2 : distance from the device center to the fixed finger's far end,

l_o : initial overlap length between movable and fixed fingers,

l_f : movable finger length,

l_r : distance from the device center to the movable finger tip.

^a: device with a circular mirror.

metallization, during which 5 nm thick Cr and 200 nm thick Au are deposited to enhance the mirror reflectivity. The radius of curvature of the mirror is > 100 nm before metallization and 45 nm after depositing the high-reflection Cr/Au coating [19].

3. Results and discussions

3.1. Resonant frequencies: modal analysis

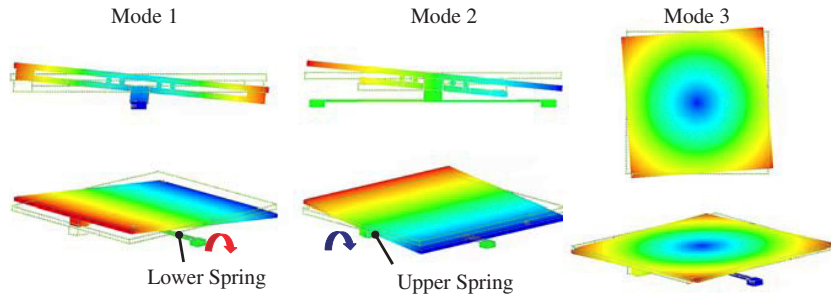
We use ANSYS, a commercial software for finite element analysis, to calculate the resonant frequencies of each device. The simulation is done without considering the metal coating. The effective spring stiffness corresponding to each eigenmode plays an important role in the device performance, e.g., pull-in voltage and maximum rotation angle. It is proportional to the square of the resonant frequency. The results of modal analysis are shown in table 2, which lists each device's lowest three mechanical resonant frequencies f_x , f_y and f_{twist} of the x -axis rotation, y -axis rotation and in-plane twist motion, respectively. For type I and type II devices, the y -axis rotation results from the upper spring torsion plus the rocking of lower springs. For each type of devices, the frequencies within a certain column vary a bit from each other as the devices'

moments of inertia are slightly different due to the different comb parameter values. We also include the squares of the frequency ratios, which are related to the spring ratios and are critical to the device performance.

3.2. DC characteristics and measured resonant frequencies

The dc characteristic, i.e. the rotation angle versus applied voltage, for each device is obtained using WYKO MHT III, a noncontact white-light interferometric surface profiler. Figure 5 is the picture of the experimental setup; the dc voltage is applied through the probes. For the measurement of device resonant frequencies, the frequencies of the ac driving voltages are swept and the optical scan angles are recorded by a position sensing detector (PSD). Table 3 summarizes the experimental results, where Θ_M , θ_M , V_{pi} and f_r denote the room for rotation, the maximum measured rotation angle, the corresponding voltage (normally the pull-in voltage except for the x -axis rotations of devices S1 and S2) and resonant frequency, respectively. The device performance strongly depends on the spring structure, initial finger gap and finger overlap length. Details will be discussed in the following sub-sections.

Table 2. Results of the modal analysis using ANSYS. The resonant frequencies of the lowest-three-order modes and the squares of the frequency ratios are listed.



Device number	Mode 1 (Hz)	Mode 2 (Hz)	Mode 3 (Hz)	f_y^2/f_x^2	f_{twist}^2/f_x^2	f_x^2/f_y^2	f_{twist}^2/f_y^2
Type I: devices with single-beam lower springs							
A1	13 147	21 339	21 074	2.63	2.57	0.38	0.98
B2	13 119	21 289	20 994	2.63	2.56	0.38	0.97
E1	13 179	21 401	21 122	2.64	2.57	0.38	0.97
B1	13 138	21 335	21 063	2.64	2.57	0.38	0.97
D1	13 229	21 463	21 197	2.63	2.57	0.38	0.98
E2	13 205	21 424	21 133	2.63	2.56	0.38	0.97
C1	13 187	21 383	21 101	2.63	2.56	0.38	0.97
D2	13 173	21 383	21 087	2.63	2.56	0.38	0.97
Type II: devices with double-beam lower springs							
D3	18 712	23 796	34 989	1.62	3.50	0.62	2.17
C3	18 645	23 705	34 890	1.62	3.50	0.62	2.16
E6	18 754	23 833	35 096	1.62	3.50	0.62	2.16
E5	18 706	23 811	35 012	1.61	3.50	0.62	2.17
E4	18 819	23 910	35 202	1.63	3.53	0.61	2.17
E3	18 711	23 864	35 134	1.61	3.50	0.62	2.17
Type III: devices with balanced cross-bar spring structures							
S1	21 345	21 385	36 427	1.00	2.91	1.00	2.90
S2	21 364	21 386	36 432	1.00	2.91	1.00	2.90
S3	26 166	26 190	48 966	1.00	3.50	1.00	3.50

Table 3. Summary of the experimental results.

Type	g (μm)	Device number	X-axis rotation				Y-axis rotation			
			Θ_M ($^\circ$)	θ_M ($^\circ$)	V_{pi} (V)	f_r (kHz)	Θ_M ($^\circ$)	θ_M ($^\circ$)	V_{pi} (V)	f_r (kHz)
I	1	A1	7.90	2.23	17.0	5.1	9.54	1.35	25.8	9.7
	1	B2		2.33	20.1	5.1		1.18	31.5	9.6
	1	A2 ^a		3.67	23.1	19.2 ^b		1.34	33.5	34.2 ^b
	2	E1		5.90	30.0	5.4		1.95	47.8	11.0
	3	D1		4.23	30.7	5.6		1.78	54.0	10.8
	3	E2		4.47	32.0	5.6		1.85	57.5	10.8
	3	C1		4.44	27.5	5.6		1.86	45.2	10.7
	3	D2		4.54	28.3	5.8		1.81	46.7	10.8
	3	C2 ^a		7.03	37.5	20.7 ^b		2.01	64.0	32.3 ^b
II	1	D3	7.90	5.46	26.1	8.1	9.54	1.61	37.3	16.8
	1	C3		5.41	31.3	7.4		1.51	44.8	12.4
	2	E6		6.68	43.0	7		2.16	65.5	12
	2	E5		5.32	45.0	8		2.13	69.9	13.5
	3	E4		4.44	45.0	7		2.65	78.0	11.2
III	3	E3	4.67	47.7	8.4	2.60	85.0	13.4		
	1	S1	6.05	5.30	50.2	11.4	11.07	6.04	52.8	11.0
	2	S2	6.05	5.51	80.6	10.7	11.42	6.95	84.2	10.4
	3	S3	7.68	5.93	95.1	14.1	10.82	5.55	102.7	14.2

^a Device with a circular mirror.

^b Measured without metal coating.

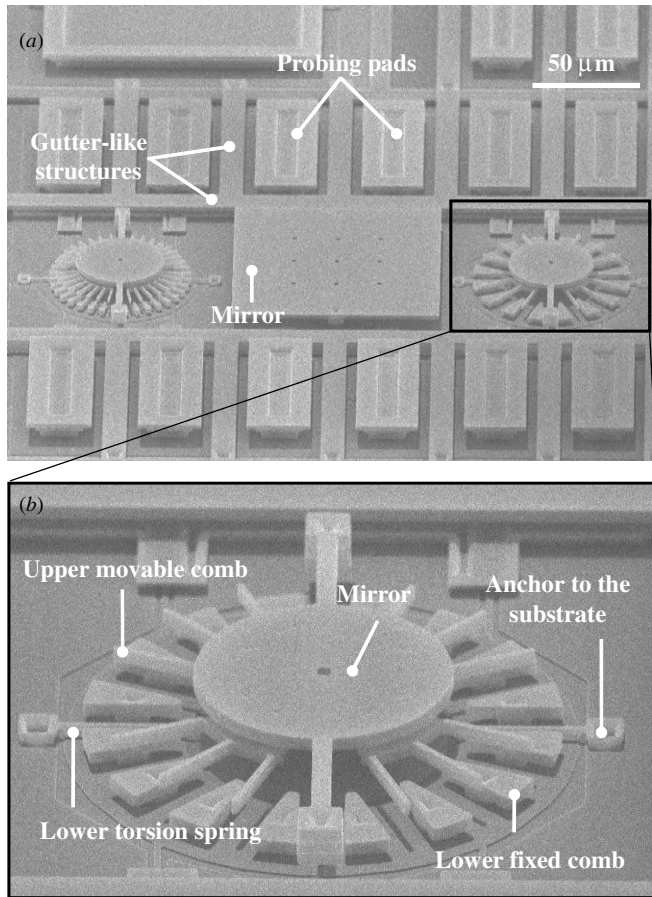


Figure 4. (a) SEM photo of typical devices and (b) a close-up of the device with a circular mirror.

3.2.1. DC characteristics of type I devices. Figures 6 and 7 show the dc characteristics of type I devices with initial finger gaps of 1 μm, 2 μm and 3 μm. Each chart has two sets of experimental data: rotation about the *x*-axis (red circular dots) and rotation about the *y*-axis (blue triangular dots). It is clear that for each device a smaller driving voltage is required for the *x*-axis rotation due to the more compliant *x*-axis torsion springs made of the thinner mmpoly1 layer. Also, the *x*-axis rotation exhibits a greater maximum scan angle, resulting in an imbalanced scan pattern.

Another feature related to the spring design is worth noting—figure 8 shows the 3D profiles of the micromirror (E1) right before pull-in under *x*- and *y*-axis actuation, demonstrating that *x*-axis tilt is induced while actuating the *y*-axis rotation. This result can be explained by a coupling-like behavior between these two modes. Since the movable and fixed combs are made by two steps of photolithography, possible fabrication deviation such as the photo mask misalignment would lead to nonuniform initial finger gap spacing. Consequently, the *x*-axis tilt is induced due to the unequal electrostatic forces acting on the movable part, even though the voltages applied on the two electrodes for driving the *y*-axis rotation are the same. From table 2 it can be seen that the ratio $f_x^2/f_y^2 (\propto k_x/k_y)$ is smaller than $f_y^2/f_x^2 (\propto k_y/k_x)$ for every type I device. This indicates that

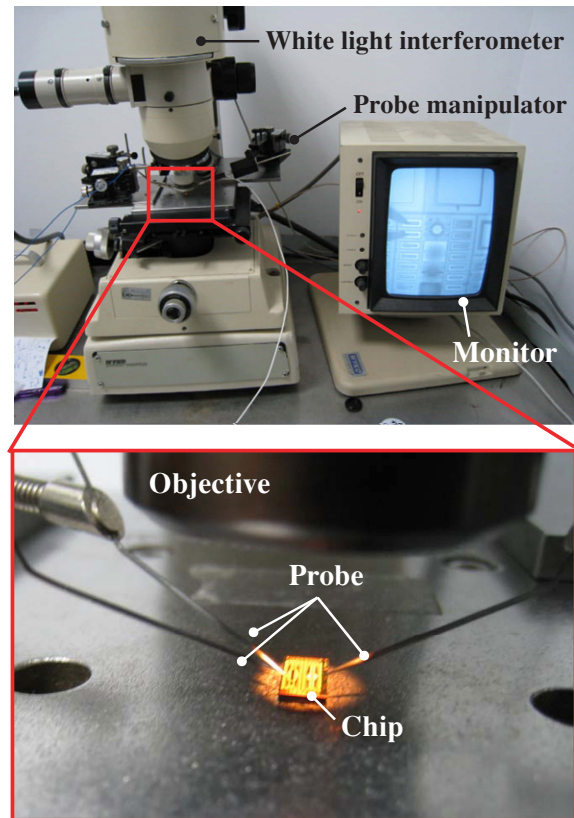


Figure 5. Picture of the experimental setup for dc characterization.

the coupling-like behavior between the *x*- and *y*-axis rotations is more pronounced under *y*-axis actuation. The detailed data of each device, i.e. the induced *x*-axis tilt amount and *y*-axis rotation angle versus applied voltage, are shown in figure 9. With a smaller initial finger gap the coupling-like behavior is more noticeable, i.e. the *x*-axis tilt can be observed at a smaller *y*-axis rotation angle. This result is supported by the fact that a device with a smaller initial finger gap is more susceptible to fabrication deviation.

In addition to the vertical comb capacitance, parallel-plate capacitance exists intrinsically between the mirror and fixed combs. The lateral instability of the comb drive and the rotational pull-in of the parallel-plate actuator compete to govern the maximum rotational angles. For the radial vertical combdrive actuator, lateral instability (also called lateral pull-in) causes an undesired twist motion which could result in contact between the movable and fixed fingers. A large ratio of k_{twist} to k_x (k_y) can effectively prevent the device from lateral pull-in, where k_x (k_y) is the spring constant of the *x*-axis (*y*-axis) rotation, and k_{twist} is the spring constant for the twist motion. Based on the mechanical resonant frequencies listed in table 2, we observe that the ratios $f_{twist}^2/f_x^2 (\propto k_{twist}/k_x)$ and $f_{twist}^2/f_y^2 (\propto k_{twist}/k_y)$ are 2.56–2.57 and 0.97–0.98, respectively. The twist mode even exhibits a slightly lower resonant frequency than that of the *y*-axis rotation, which implies the *y*-axis rotation is more susceptible to the lateral instability due to the lower k_{twist}/k_y ratio. The finger gap is another critical parameter determining the degree of the lateral instability. This is particularly conspicuous for

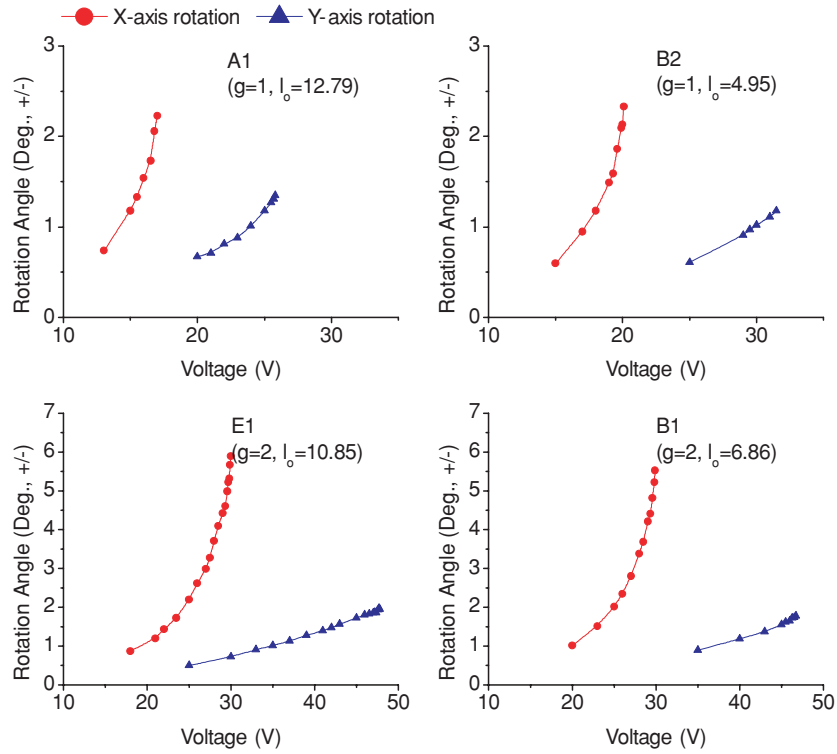


Figure 6. Measured dc characteristics of type I devices with initial finger gaps of 1 μm and 2 μm .

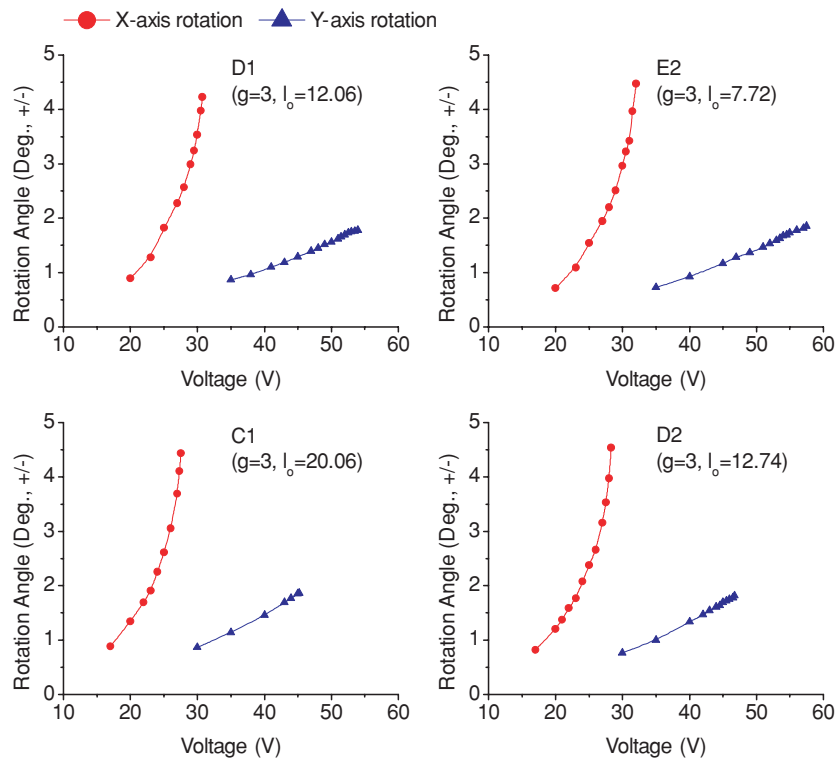


Figure 7. Measured dc characteristics of type I devices with an initial finger gap of 3 μm .

radial comb drive since the finger gap spacing within a single device alters nonuniformly during rotation. A smaller initial finger gap results in a greater degree of lateral instability.

Figures 10(a) and (b) summarize the dc characteristics of the eight type I devices for the x - and y -axis rotations, respectively. Basically, a device with a smaller initial finger

gap requires a lower driving voltage to tilt the micromirror to a certain angle. This result agrees with the fact that a smaller finger gap leads to a larger force density. Particularly, for our radial combdrive design, the device with a smaller finger gap also possesses more fingers, further increasing the electrostatic torque.

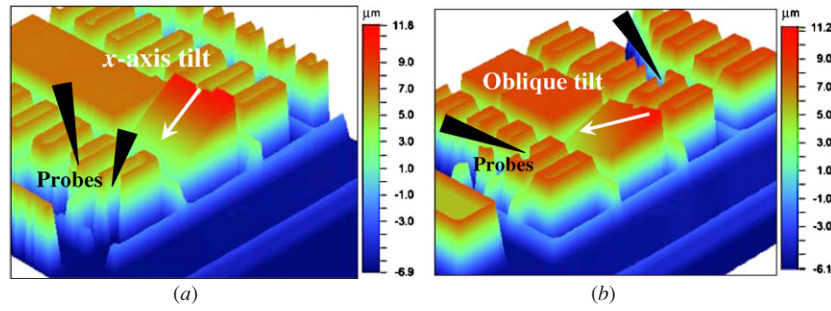


Figure 8. 3D profiles of the micromirror (E1) right before pull-in under (a) x-axis and (b) y-axis actuation.

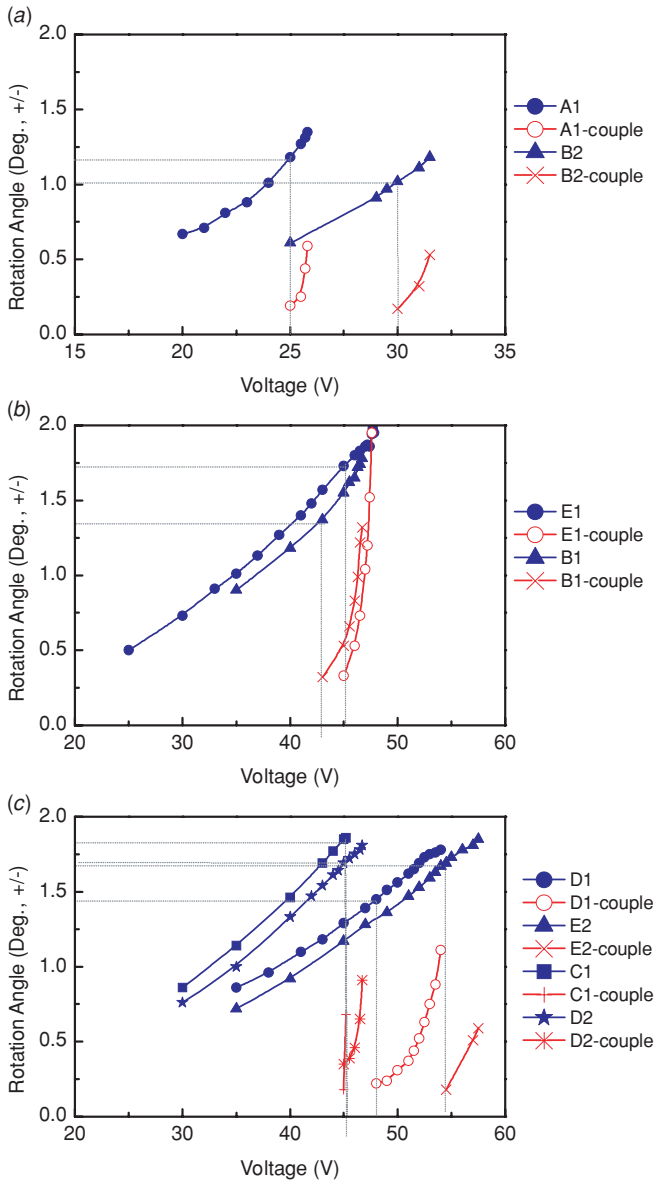


Figure 9. The y-axis rotation angle and induced x-axis tilt (labeled with 'couple') under y-axis actuation for type I devices with initial finger gaps of (a) 1 μm , (b) 2 μm and (c) 3 μm .

For the x-axis rotation, devices with an initial gap of 1 μm are verified to experience lateral pull-in whereas those with finger gaps of 2 μm and 3 μm are governed by the rotational pull-in. Figure 11(a) is the microscope image of

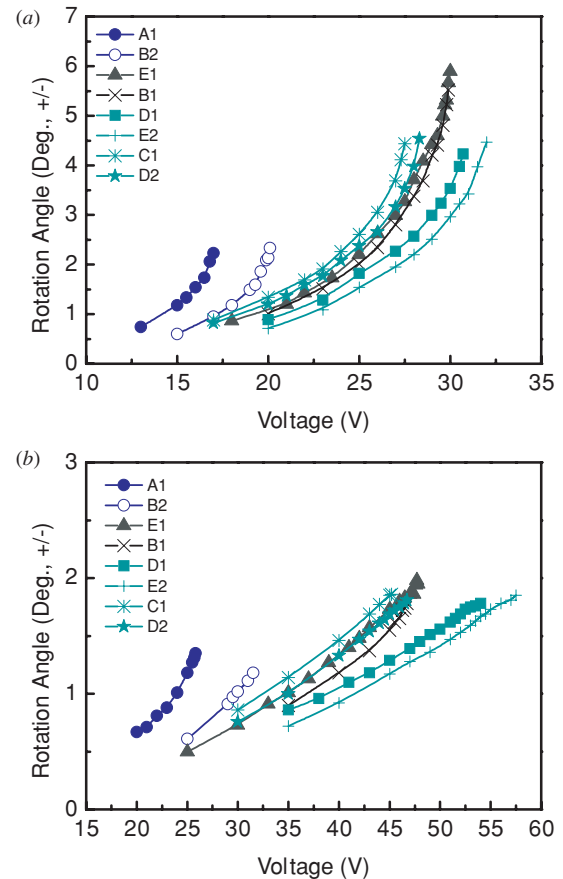


Figure 10. Comparison between the dc characteristics of the eight devices of type I for the (a) x-axis rotation and (b) y-axis rotation.

device B2 after pull-in under x-axis actuation. It exhibits a twist, indicating that the moving comb fingers are laterally pulled toward the fixed fingers due to lateral instability. This phenomenon is not observed in devices with a gap of 2 μm or 3 μm (see figure 11(b)). Therefore, the maximum mechanical scan angles for the x-axis rotation of devices A1 and B2 (1 μm initial finger gap) are only 2.23° and 2.33°, respectively, which are much smaller than those of other devices. The angles of the 2 μm gap devices are greater than those of the 3 μm gap ones. This is because the 2 μm gap devices have larger comb capacitance, suppressing the contribution of the parallel-plate capacitance which causes the rotational pull-in. For the

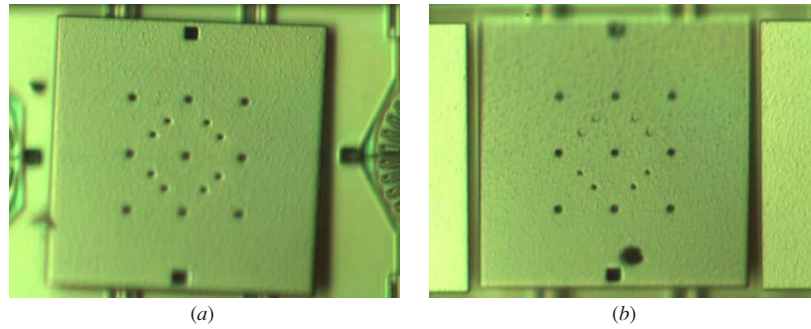


Figure 11. Microscope images taken after pull-in under x -axis actuation for (a) device B2 (type I device with initial finger gap = $1 \mu\text{m}$) and (b) device B1 (type I device with initial finger gap = $2 \mu\text{m}$).

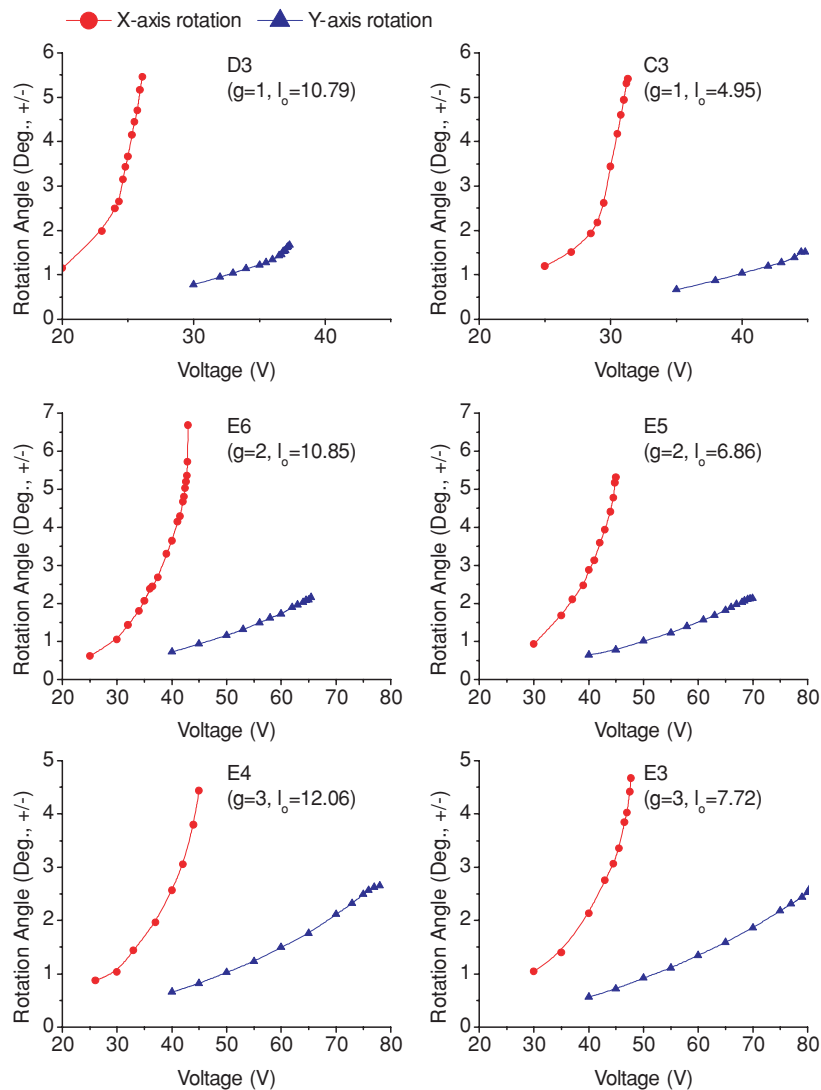


Figure 12. Measured dc characteristics of type II devices with initial finger gaps of $1 \mu\text{m}$, $2 \mu\text{m}$ and $3 \mu\text{m}$.

devices with a gap of $3 \mu\text{m}$, the required voltages for C1 and D2 are less than those for D1 and E2 because C1 and D2 have larger l_2 and l_o , which leads to stronger electrostatic torques.

For the y -axis rotation, the scan angles of all devices are determined by the lateral instability due to the smaller k_{twist}/k_y . As anticipated, the $1 \mu\text{m}$ devices exhibit the smallest y -axis rotation angles. Moreover, the maximum angle of the y -axis

rotation is smaller than that of the x -axis rotation for each device.

3.2.2. DC characteristics of type II devices. Figure 12 shows the dc characteristics of type II devices. The comparison between devices for both the x - and y -axis rotations is demonstrated in figure 13. Resembling the type I devices

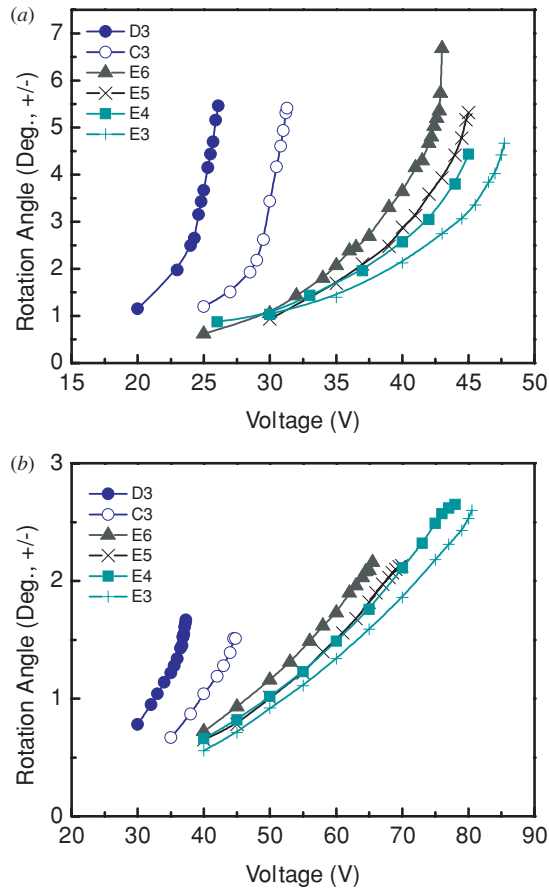


Figure 13. Comparison between the dc characteristics of the six devices of type II for the (a) x -axis rotation and (b) y -axis rotation.

in the imbalanced scan patterns, the type II devices require even higher driving voltages due to the greater stiffness of the double-beam lower springs. However, the employment of the double-beam lower springs not only increases the resistibility against lateral pull-in, but also suppresses the coupling-like behavior between the x - and y -axis rotations. This can be theoretically predicted by the ANSYS modal analysis. From table 2, we find that the ratios $f_{\text{twist}}^2/f_x^2 (\propto k_{\text{twist}}/k_x)$ and $f_{\text{twist}}^2/f_y^2 (\propto k_{\text{twist}}/k_y)$ of type II devices are improved to 3.50–3.53 and 2.16–2.17, respectively. The ratio $f_x^2/f_y^2 (\propto k_x/k_y)$ is also increased from 0.38 to 0.61–0.62.

The experimental data also confirm these enhancements. As observed in figure 13, devices with an initial finger gap of 1 μm (C3 and D3) achieve larger x -axis rotation angles in comparison with their counterparts of type I, even though they are still subject to lateral instability. Parallel-plate rotational pull-in still governs the devices with finger gaps of 2 μm and 3 μm . E6 and E5 (initial finger gap = 2 μm) exhibit larger angles than E4 and E3 (initial finger gap = 3 μm) as explained earlier. Although the y -axis rotations of all type II devices still experience lateral pull-in, larger angles are achieved thanks to the better lateral stability. However, the maximum angle of y -axis rotation is still smaller than that of x -axis rotation for each device.

Along with the improvement of lateral stability comes the suppression of the coupling-like behavior between the x - and

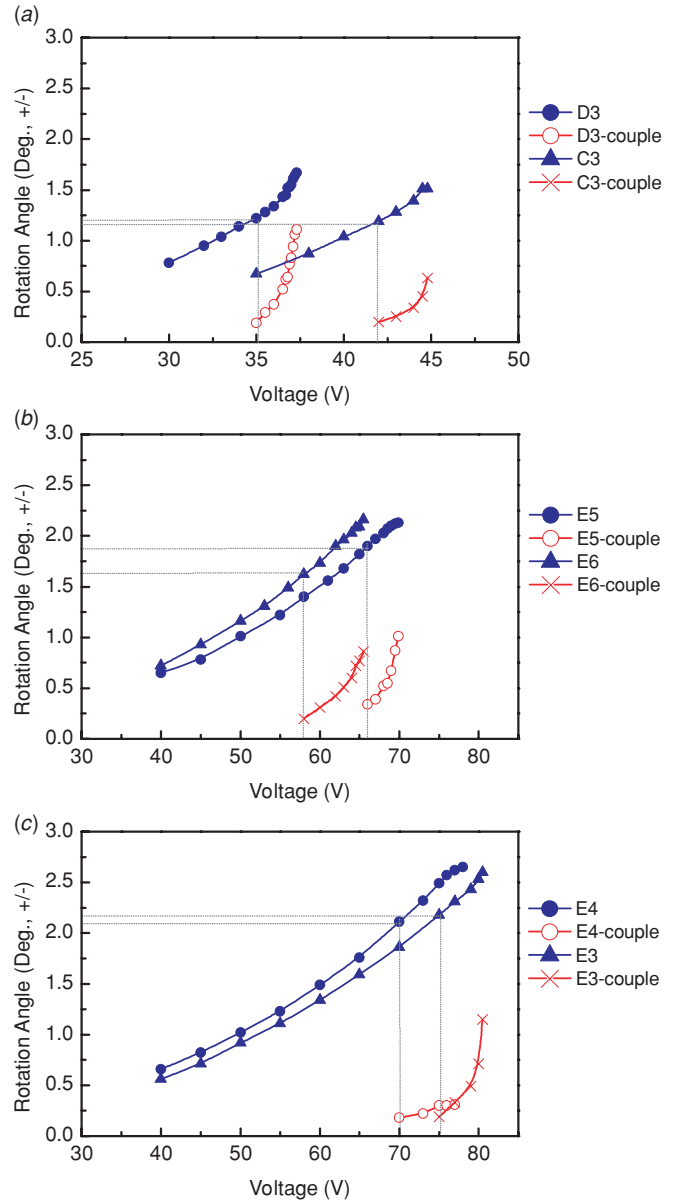


Figure 14. The y -axis rotation angle and induced x -axis tilt (labeled with ‘couple’) under y -axis actuation for type II devices with initial finger gaps of (a) 1 μm , (b) 2 μm and (c) 3 μm .

y -axis rotations. As shown in figure 14, each type II device experiences the induced x -axis tilt under the y -axis actuation later than its type I counterpart with the same initial gap.

3.2.3. DC characteristics of type III devices. Figure 15 shows the dc characteristics of each device of type III. With modification of the cross-bar spring into a balanced structure, the primary two orthogonal rotational modes become degenerate, and therefore we are able to achieve identical x - and y -axis scan ranges. As shown in table 2, the resonant frequencies of the two primary rotational modes for each device are almost the same as expected. The lateral stability is also improved due to the shorter torsion spring design. The ratios $f_{\text{twist}}^2/f_x^2 (\propto k_{\text{twist}}/k_y)$ and $f_{\text{twist}}^2/f_y^2 (\propto k_{\text{twist}}/k_x)$ are 2.91, 2.91 and 3.50 for devices S1, S2 and S3, respectively.

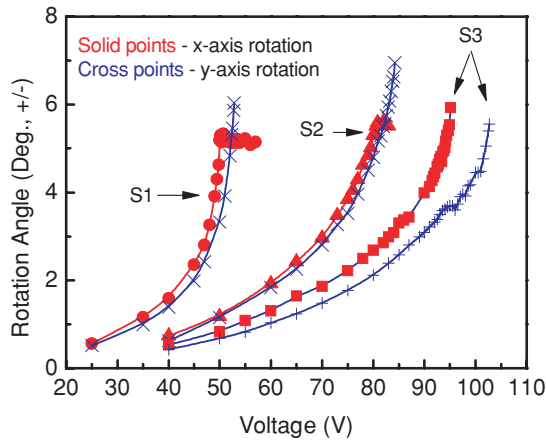


Figure 15. Comparison between the dc characteristics of the three devices of type III.

Thanks to the excellent lateral stability, the scan ranges of both the *x*- and *y*-axis rotations reach large angles. Besides, no significant coupling-like behavior between the *x*- and *y*-axis rotations is observed. For devices S1 and S2, the *x*-axis rotation reaches the maximum angle when the far end of the *y*-axis spring touches the shielding ground plane. Their *x*-axis rotation ranges are 5.30° and 5.51° , respectively. These angles are smaller than the ideal maximum rotation room (6.05°) for two possible reasons: deviation of the thickness of the sacrificial SiO_2 layer from the nominal value $2 \mu\text{m}$ and the sagging accompanied by the rotation motion. The sagging occurs as the electrostatic force exerting on the movable part not only provides a torque but also a net downward force.

3.2.4. DC characteristics of the devices with circular mirrors.

Figures 16(a) and (b) each compare devices that have the same spring structure and comb design but different mirror shapes (square and circular). With the mirrors intentionally cut into circular shapes, devices A2 and C2 bear almost no parallel-plate capacitance and are mainly driven by the radial vertical comb drives. They require higher driving voltages than their counterparts (B2 and D2) with square mirrors due to the lack of the parallel-plate capacitance between the mirror and fixed combs. As shown in figure 16, the characteristic difference between A2 and B2 ($1 \mu\text{m}$ finger gap) is less significant than

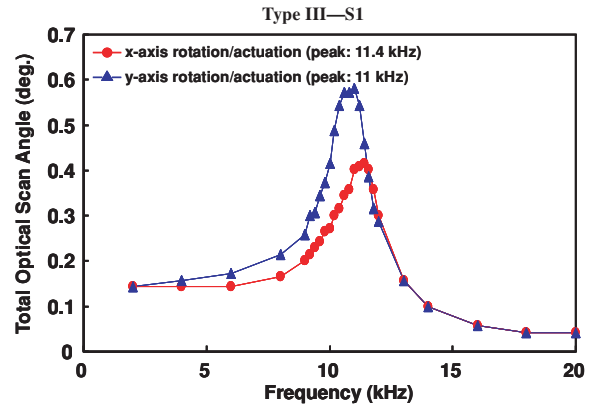


Figure 17. Frequency responses of device S1.

that between C2 and D2 ($3 \mu\text{m}$ finger gap). This is attributed to the fact that for devices with a smaller finger gap a major portion of the total capacitance comes from the contribution of the comb drives. In other words, the combdrive actuators dominate the characteristics of such devices. Therefore, the mirror shape appears to be a less important factor for small-gap devices.

3.2.5. Resonant frequencies.

The measured resonant frequencies for the *x*-axis and *y*-axis rotations are also included in table 3. The resonant frequencies obtained by experimental measurement are respectively smaller than their counterparts as calculated by the simulation. This is due to the additional moments of inertia resulting from the metal coating and the reduced spring widths caused by the over-etching at the springs during the fabrication process. Moreover, among devices of the same type, the measured frequencies for rotation about a certain axis differ. This is because the devices' moments of inertia are not exactly the same due to the different comb parameter values, and the probable etching nonuniformity can lead to different degrees of spring over-etching. The circular mirrors exhibit significantly greater resonant frequencies thanks to their much smaller moments of inertia and the absence of metal coating. The frequency responses of device S1 are shown in figure 17. The resonance peaks for the *x*- and *y*-axis rotations are located at 11.4 kHz and 11 kHz, respectively.

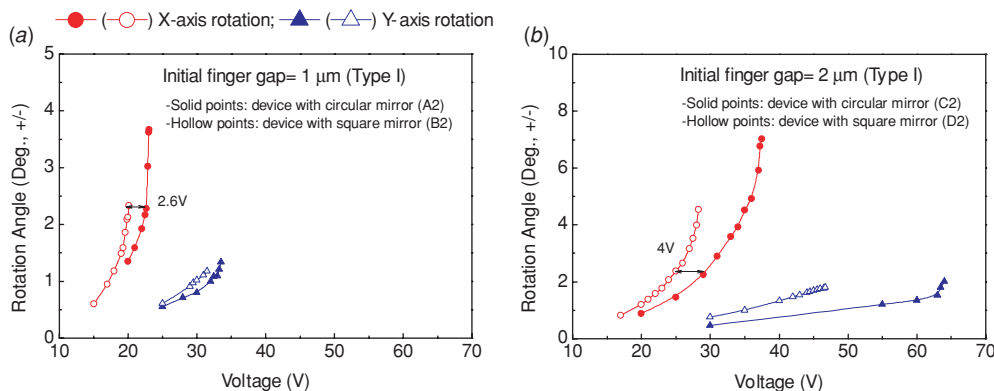


Figure 16. DC characteristic comparison between the devices with square mirrors and those with circular mirrors.

4. Conclusions

Novel two-axis MEMS scanners with radial vertical combdrive actuators have been demonstrated in this paper. The devices are designed based on a five-layer polysilicon surface micromachining process. The cross-bar spring structure consisting of x -axis and y -axis torsion springs is incorporated to achieve two rotational degrees of freedom, enabling the dual-axis scanning. With the radial comb drives and cross-bar spring structure hidden underneath the mirror, the scanner can be replicated to form 1D or 2D arrays with high fill factors. Experiments on devices of different designs are performed and the results are analyzed.

The optimal design (S1) comes with a balanced cross-bar spring structure. The mechanical rotation angles are $\pm 5.30^\circ$ (50.2 V) and $\pm 6.04^\circ$ (52.8 V) for rotations about the x and y axes, respectively. For each rotational mode, a significant angle is obtained under a reasonable bias voltage. The resonant frequencies are 11.4 kHz and 11 kHz.

Acknowledgments

This work was supported by the National Science Council of Taiwan under grants NSC 95-2221-E-002-053 and NSC 96-2221-E-002-198-MY2, and Excellent Research Projects of National Taiwan University, 95R0062-AE00-06 and 97R0062-07. The authors would also like to thank Professor Long-Sun Huang of Institute of Applied Mechanics, National Taiwan University, for the access to WYKO.

References

- [1] Aksyuk V A et al 2003 238×238 micromechanical optical cross connect *IEEE Photonics Technol. Lett.* **15** 587–9
- [2] Chu P B et al 2005 Design and nonlinear servo control of MEMS mirrors and their performance in a large port-count optical switch *J. Microelectromech. Syst.* **14** 261–73
- [3] Aksyuk V A et al 2003 Beam-steering micromirrors for large optical cross-connects *IEEE J. Lightwave Technol.* **21** 634–42
- [4] Ducellier T et al 2004 Novel high performance hybrid waveguide-MEMS 1×9 wavelength selective switch in a 32-cascade loop experiment *Proc. European Conf. on Optical Communication (ECOC 2004) (Stockholm, Sweden, September 2004)* Paper Th4.2.2
- [5] Milanović V, Castelino K and McCormick D T 2007 Highly adaptable MEMS-based display with wide projection angle *Proc. 2007 IEEE Int. Conf. on Micro Electro Mechanical Systems (Kobe, Japan)* pp 143–6
- [6] Yalcinkaya A D, Urey H, Brown D, Montague T and Sprague R 2006 Two-axis electromagnetic microscanner for high resolution displays *J. Microelectromech. Syst.* **15** 786–94
- [7] Murakami K, Murata A, Suga T, Kitagawa H, Kamiya Y, Kubo M, Matsumoto K, Miyajima H and Katashiro M 2003 A miniature confocal optical microscope with MEMS gimbal scanner *Proc. The 12th Int. Conf. on Solid State Sensors, Actuators and Microsystems (Boston, MA, 8–12 June)* pp 587–90
- [8] Kim J H, Lee H K, Kim B I, Jeon J W, Yoon J W and Yoon E 2003 A high fill-factor micro-mirror stacked on a crossbar torsion spring for electrostatically-actuated two-axis operation in large-scale optical switch *Proc. 2003 IEEE Int. Conf. on Micro Electro Mechanical Systems (Kyoto, Japan)* pp 259–62
- [9] Bochobza-Degani O and Nemirovsky Y 2004 Experimental verification of a design methodology for torsion actuators based on a rapid pull-in solver *J. Microelectromech. Syst.* **13** 121–30
- [10] Xie H, Pan Y and Fedder G K 2003 A CMOS-MEMS mirror with curled-hinge comb drives *J. Microelectromech. Syst.* **12** 450–7
- [11] Kim J, Choo H, Lin L and Muller R S 2006 Microfabricated torsional actuators using self-aligned plastic deformation of silicon *J. Microelectromech. Syst.* **15** 553–62
- [12] Conant R A, Nee J T, Lau K Y and Muller R S A flat high-frequency scanning micromirror pp 6–9 Technical Digest of 2000 Solid-State Sensor and Actuator Workshop (Hilton Head, SC, USA)
- [13] Tsou C, Lin W T, Fan C C and Chou Bruce C S 2005 A novel self-aligned vertical electrostatic combdrives actuator for scanning micromirrors *J. Micromech. Microeng.* **15** 855–60
- [14] Lim T S, Ji C H, Oh C H, Kwon H, Yee Y and Bu J U 2004 Electrostatic MEMS variable optical attenuator with rotating folded micromirror *IEEE J. Sel. Top. Quantum Electron.* **10** 558–62
- [15] Ra H, Piyawattanametha W, Taguchi Y, Lee D, Mandella M J and Solgaard O 2007 Two-dimensional MEMS scanner for dual-axes confocal microscopy *J. Microelectromech. Syst.* **16** 969–76
- [16] Milanovic V, Matus G A and McCormick D T 2004 Gimbal-less monolithic silicon actuators for tip-tilt-piston micromirror applications *IEEE J. Sel. Top. Quantum Electron.* **10** 462–71
- [17] Pardo F et al 2007 Flexible fabrication of large pixel count piston-tip-tilt mirror arrays for fast spatial light modulators *Microelectron. Eng.* **84** 1157–61
- [18] Chiou S-J, Hsieh T-L, Tsai J C, Sun C W, Hah D and Wu M C 2007 A two-axis MEMS scanner driven by radial vertical combdrive actuators *IEEE/LEOS Int. Conf. on Optical MEMS and Nanophotonics (Hualien, Taiwan, 12–16 August 2007)* pp 83–4
- [19] Tsai J C, Chiou S-J, Hsieh T-L, Sun C W, Hah D and Wu M C 2008 Two-axis MEMS scanners with radial vertical combdrive actuators—design, theoretical analysis, and fabrication *J. Opt. A: Pure Appl. Opt.* **10** 044006
- [20] Hsieh T L, Chang Y T, Chiou S J, Tsai J C, Hah D and Wu M C 2008 Performance improvement of a two-axis radial-vertical-combdrive scanner by using a symmetric spring design *IEEE/LEOS Int. Conf. on Optical MEMS and Nanophotonics (Freiburg, Germany, 11–14 August 2008)* pp 108–9